

Article

Enhancement of the Corrosion Resistance of 304 Stainless Steel by Cr–N and Cr(N,O) Coatings

Mihaela Dinu ¹, Emile S. Massima Mouele ², Anca C. Parau ¹, Alina Vladescu ^{1,3} , Leslie F. Petrik ²  and Mariana Braic ^{1,*}

¹ National Institute for Optoelectronics, 409 Atomistilor St., 077125 Magurele, Romania; mihaela.dinu@inoe.ro (M.D.); anca.parau@inoe.ro (A.C.P.); alinava@inoe.ro (A.V.)

² Department of Chemistry, Environmental and Nano Sciences, University of the Western Cape, Robert Sobukwe Road, Bellville 7535, South Africa; 2916096@myuwc.ac.za (E.S.M.M.); lpetrik@uwc.ac.za (L.F.P.)

³ National Research Tomsk Polytechnic University, Lenin Avenue 43, Tomsk 634050, Russia

* Correspondence: mariana.braic@inoe.ro; Tel.: +4-21-457-57-59

Received: 27 February 2018; Accepted: 2 April 2018; Published: 5 April 2018



Abstract: Chromium nitride and oxynitride coatings were deposited as monolayers ((Cr–N), Cr(N,O)) and bilayers (Cr–N/Cr(N,O), Cr(N,O)/Cr–N) on 304 steel substrates by reactive cathodic arc method. The coatings were characterised by X-ray diffraction (XRD), scanning electron microscopy (SEM), energy dispersive X-ray spectrometry (EDS), surface profilometry, and scratch tester. The anticorrosive properties of the coatings were assessed by electrochemical tests in 0.10 M NaCl + 1.96 M H₂O₂, carried out at 24 °C. Cr₂N, CrN, and Cr(N,O) phases were identified in the coatings by grazing incidence X-ray diffraction (GI-XRD) measurements. The measured adhesion values ranged from 19 N to 35 N, the highest value being obtained for the bilayer with Cr(N,O) on top. Electrochemical tests showed that Cr(N,O) presence in both mono- and bilayered coatings determined the lowest damage in corrosive solution, as compared to the Cr–N coatings. This improvement was ascribed to the more compact structure, lower coatings porosity, and smoother surface.

Keywords: chromium nitride; chromium oxynitride; multilayer; cathodic arc deposition; corrosion resistance; coating adhesion

1. Introduction

For the past decades, material science has emerged as one of the major scientific fields aiming at the improvement of the physical and chemical properties of materials, taking their projected purpose into consideration. The stainless steel (SS) family represents one of the most utilized alloys, being used in a wide range of applications, such as cutting tools, convenient support in biomedicine, rotor blades of gas turbines, aircraft parts, automobiles, pipelines, and naval vessels [1–20]. The selection of the specific SS to be used in a certain application is done considering the economic aspects as well as its physical and chemical properties. An excessive amount of transition metals (TMs) such as Cr and Fe in SS alloys may influence the chemical stability. The abundance of Cr in SS alloy may largely contribute to the formation of a passive Cr₂O₃ layer, acting as a corrosion-protective layer. However, an excessive amount of Fe in SS alloy may induce its oxidation to FeO, which accelerates SS rusting [21]. More often, the chemical stability of alloys is either temperature- or pH-dependent [20,22,23]. The exposure of SS to such harsh environments may result in corrosion that further limits its performance and durability [6,20,24]. Even though various approaches to corrosion prevention have been proposed in the literature [16], they might be costly.

The use of coatings containing carbon, oxygen, or nitrogen (e.g., carbides, nitrides, carbonitrides, or oxynitrides) has become a practical method used to improve the performance of SS [15,17–20,24].

Coatings designed to withstand corrosion are already in use in various fields, such as orthopaedics, dentistry, tribology, and photocatalysis. In order to enhance the performance of SS, numerous anticorrosion solutions have been developed based on coating application by the pulse laser deposition (PLD) or cathodic arc deposition (CAE) [14]. While large area coatings are still difficult to produce economically by PLD, CAE is a high-productivity method, producing an intense plasma flux at the cathode spots generated by the electric arc. The arc plasma comprises an important fraction of single or multiple ionized atoms. This peculiarity is of great importance, since the bombardment of the growing film by energetic ions and neutrals creates a highly adhesive coating, which can ensure the integrity of the coated structure in the long term [25,26]. Another particularity of the CAE method consists of the significant roughness of the coated surfaces, resulting from droplets ejected by the cathode due to its local melting. Considering this issue, different techniques have been developed, including venetian blinds, magnetic shielding, increased deposition pressure, as well as the development of more sophisticated methods consisting mainly of short-pulsed voltage applied on the substrate [27–31].

Therefore, understanding the corrosion behaviour of coated materials is an important step in achieving the maximum protection of coated materials and hence boosting their life service in chemically aggressive environments [12–14,16,32]. Based on the reported results, various corrosion-resistant coatings have been developed to improve the corrosion resistance of SS. Different TM nitride coatings have been synthesised and investigated due to their high hardness, good oxidation resistance, and low wear rate in dry atmosphere, as well as their phase stability in corrosive environments [10,15,33–37]. Oxynitride coatings have also been studied due to their plasmonic properties, relatively low electrical resistivity, good biocompatibility, and high oxidation resistance [25,38–46].

The aim of the present study was to develop rough, large surface area, corrosion- and erosion-resistant coatings for 304 stainless steel mesh, used as support for powder photocatalysts, utilised in water remediation technologies [47]. The first step was to ascertain the corrosion behaviour of such coatings deposited on solid pieces of 304 stainless steel in relation to other properties, such as crystalline structure, mechanical properties, and surface roughness.

In the current study, we report on the electrochemical behaviour of Cr nitride and oxynitride coatings deposited on 304 SS substrates by CAE technique, as there is abundant scientific literature about the use of Cr-based coatings in severe environments, due to their superior corrosion resistance [45,48–54]. The corrosion tests of the plain and coated SS were carried out in saline solution by potentiodynamic polarization technique. The corrosion performance of the coatings was examined in relation to the coatings features, such as elemental and phase composition, surface morphology, hardness, reduced elastic modulus, and adhesion to SS substrate.

2. Materials and Methods

The Cr-based coatings (nitride and oxynitride) were prepared on 304 SS discs ($\Phi = 20$ mm) and Si pieces (20×20) mm² by the reactive CAE, using a Cr cathode (99.5% purity, Cathay Advanced Materials Ltd., Guangdong, China).

The chemical composition of the 304 SS, as given by the manufacturer in wt.% and at.%, is presented in Table 1.

Each 304 SS substrate was sanded using a SiC abrasive paper (grit 800), polished ($R_a = 60$ nm), ultrasonically washed in isopropyl alcohol and water for 10 min, then dried at 120 °C for 1 h.

For controlling the coating uniformity, the samples were placed on a rotating sample holder. Moreover, before deposition, the substrates were sputter etched with Ar⁺ for 5 min to remove any contaminant layer. The residual pressure in the system was 2×10^{-3} Pa. The total gas pressure during the deposition was 8×10^{-2} Pa. For the nitride coatings, nitrogen was introduced in the chamber at a mass flow rate of 60 sccm, while for the oxynitrides, the same value of the nitrogen mass flow rate was used, and 17 sccm of the oxygen was added. The arc current applied on the Cr cathode was 90 A, and the substrates were biased at -200 V. This value was selected based on our previous studies [55], aiming for the enhancement of coatings' corrosion resistance. As previously reported, by selecting the

appropriate value for the bias voltage, the coatings' properties can be tuned, mainly related to their crystallinity and surface roughness [56]. For the bilayer coatings, the same deposition parameters were used. However, the deposition time of each individual layer was modified in order to obtain almost the same thickness for all the coatings, around 1 μm .

Table 1. Chemical composition of 304 L stainless steel (wt.% and at.%).

Composition	Element										
	Fe	C	Mn	Si	Cr	Ni	P	S	Co	Mo	Cu
wt.%	70.976	0.004	1.220	0.208	17.746	8.524	0.020	0.014	0.160	0.589	0.539
at.%	70.380	0.020	1.230	0.410	18.900	8.040	0.036	0.024	0.150	0.350	0.470

The thickness and the surface roughness of the coatings were investigated using a Dektak 150 surface profilometer (Bruker, Billerica, MA, USA) equipped with a 2.5 μm radius stylus. The thickness of the coatings was measured by surface profilometry according to the standard DD ENV1071-1:1994 [57], as follows. Part of a Si substrate was masked, such that an edge was formed during the deposition. Ten lines transverse to this edge were scanned at a scan rate of 20 $\mu\text{m}/\text{s}$, resulting in different heights; the averaged value was considered as the mean thickness of the film. The roughness of each SS sample was determined before and after the corrosion testing using the same 2.5 μm radius stylus, moving over a length of 10 mm at a scan rate of 50 $\mu\text{m}/\text{s}$. The roughness of all the investigated specimens (substrate and coatings) was evaluated based on two roughness parameters: the arithmetic average deviation from the mean line (R_a) and the root mean square average of the profile heights over the evaluation length (R_q). Moreover, the asymmetry of the profile about the mean line was also considered by calculating the skewness parameter (S_k). The presented roughness values represent the average data obtained from 5 measurements (10 mm length), performed on different areas of each specimen. After the corrosion tests, the profilometry measurements were also carried out on the substrate and all the coatings for visualisation of the significant profiles of the resulted pits.

A scanning electron microscope (SEM) (Hitachi TM3030 Plus, Tokyo, Japan) coupled with an energy dispersive X-ray spectrometer (EDS) (Bruker, Billerica, MA, USA), operated at an accelerating voltage of 15 kV, was used for the surface morphology and elemental composition investigation of the bare and coated substrate. For EDS, measurements were performed on 10 different areas of (298 \times 217) μm^2 , before and after the corrosion tests. The arithmetic mean and the standard deviation were then calculated. Images of the surface morphology for each specimen were recorded at both 30 \times and 100 \times magnification. Moreover, for the identification of corrosion products, images of element mapping were also acquired in different areas of each specimen's surface.

The phase composition of the samples was investigated by X-ray diffraction (XRD) using a SmartLab diffractometer (Rigaku, Tokyo, Japan), with a Cu K α radiation ($\lambda = 0.15405$ nm). Grazing incidence scans in the range 30 $^\circ$ –70 $^\circ$ at 2 $^\circ$ incidence, with a step size of 0.02 $^\circ$ were obtained for the coatings deposited on Si and SS substrates.

A Hysitron TI Premier nanoindenter, equipped with a Berkovich diamond tip (100 nm radius), was used for the nanoindentation measurements, for obtaining the hardness (H) and the reduced modulus (E_r) values. The normal force used was 5 mN to obtain individual indents for penetration depths in the 50–80 nm range. In order to take the possible imperfections of the indenter into account, the system was calibrated before indentation measurements using a standard fused quartz piece. Five indentations were done at the same force for each measurement, which were positioned at least 12 μm apart in order to prevent the effects of any possible interference between the indentation points. The Oliver–Pharr method was used to extract hardness (H) and reduced elastic modulus (E_r) values from the load–displacement curves [58].

The corrosion resistance was evaluated by the potentiodynamic techniques in 0.10 M NaCl + H₂O₂ (pH = 4), at room temperature (24 $^\circ\text{C}$), using a VersaStat 3 Potentiostat/Galvanostat (Princeton Applied

Research, Oak Ridge, TN, USA). A typical three-electrode cell was used, with a Pt counter-electrode and an Ag/AgCl reference electrode. The coated and uncoated (used as control) stainless steels were used as working electrode, being placed in a Teflon holder with a working area of 1 cm². Firstly, the open circuit potential (E_{OC}) was monitored for 15 h after immersion. To identify the polarisation resistance (R_p), a linear polarisation technique was used by applying a perturbation potential of -0.01 to 0.01 V vs. E_{OC} at a scanning rate of 1 mV/s. R_p parameter was determined as the slope of the linear region of the $\Delta E - \Delta i$ curve at corrosion potential (E_{corr}). Further, Tafel plots were recorded from -0.25 V to 0.25 V vs. E_{OC} at a scanning rate of 1 mV/s. The E_{corr} parameter, anodic (β_a) and cathodic (β_c) slopes, and corrosion current density (i_{corr}) were extracted from Tafel plots. The porosity (P) was estimated from Elsener's empirical equation (Equation (1)) based on the polarisation resistance of the uncoated (R_{ps}) and coated (R_{pc}) SS specimen, the difference between the corrosion potentials of the coated and uncoated SS specimen (ΔE_{corr}) and corresponding anodic slope (β_a).

$$P = \left(\frac{R_{ps}}{R_{pc}} \right) \times 10^{\frac{-|\Delta E_{corr}|}{\beta_a}} \quad (1)$$

The protective efficiency (P_e) was also calculated (Equation (2)) based on the corrosion current densities of the coatings (i_{corr_c}) and the SS specimen (i_{corr_s}):

$$P_e = \left(1 - \frac{i_{corr_c}}{i_{corr_s}} \right) \times 100 \quad (2)$$

Scratch tests under standard conditions (indenter—0.2 mm radius diamond tip, load—continuous increase from 0 to 100 N, scratching speed—10 mm/min, scratching distance—10 mm) were undertaken to determine the coating adhesion, using a laboratory system. The critical loads values at which the film flaking starts (L_1) and at which the delamination is completed (L_2) were determined by optical microscopy.

The coatings were labelled considering the left written coating, being near the substrate, such as in Cr-N/Cr(N,O) bilayer, the top layer being Cr(N,O).

3. Results and Discussion

3.1. Surface Morphology and Elemental Composition before Corrosion Measurements

Representative SEM micrographs of Cr-N and Cr(N,O) coatings are presented in Figure 1. As expected in CAE deposition, microdroplets can be noticed over the surface of all the investigated specimens—more evident in the Cr-N coating, while the Cr(N,O) coating presents a smoother surface, as seen in the magnified images. The same results were reported by Li Ming-sheng on the reactive CAE deposition of chromium in nitrogen and oxygen atmosphere [59]. It was documented by Munz that a cathode material with low melting temperature (T_m) generates an increased number of droplets with larger size [60]. The observed differences in roughness may be explained by the difference between the T_m of Cr and its compounds: $T_m^{Cr_2N}$ (1923 K) < T_m^{CrN} (2043 K) < T_m^{Cr} (2143 K) < $T_m^{Cr_2O_3}$ (2708 K), as documented by the binary phase diagrams of Cr-N and Cr-O [61]. The process is related to the temporary formation of small islands of the reactive compounds on the cathode surface due to the dense plasma arc condition. The islands are melted by the steering arc, such that the resulting microdroplets are propelled to the substrate. In a nitrogen atmosphere, the surface of the metallic Cr cathode is covered with Cr_2N and CrN, and mainly with CrN or even Cr_2O_3 if the deposition atmosphere consists of a mixture of oxygen and nitrogen, as a direct result of the higher reactivity of oxygen compared to the nitrogen molecule. It is reasonable to believe that the observed difference in surface roughness of Cr-N and Cr(N,O) coatings is related to the different T_m of the reactive compounds formed on the cathode as a result of metal target poisoning in reactive CAE.

Despite this peculiarity, the surface of both coatings was uniform, without major morphological defects such as pores, pinholes, and voids, proven as deleterious for corrosion protection of the steel substrate.

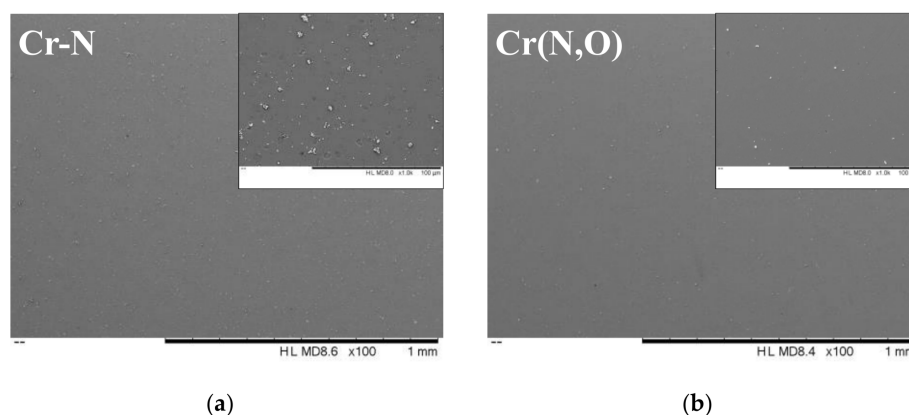


Figure 1. SEM micrographs of the investigated monolayers before the corrosion tests: (a) Cr–N; (b) Cr(N,O).

For each type of coating, the averaged values of the atomic concentrations, together with O/N, O/Cr, and (O + N)/Cr concentration ratios, are presented in Table 2. As standard samples were not available, the accepted precision in EDS measurement was defined as the relative standard deviation: $RDS (\%) = (\delta_{at}/C_{am}) \times 100$, where δ_{at} represents the calculated *SD* (%) of 10 measurements, and C_{am} represents the arithmetic mean concentration of the constituent element. In order to improve the accuracy of the results, long counting (acquisition) times were used [46,47]. To improve the accuracy of the light elements concentration, the low-energy domain of each spectrum was deconvoluted, considering the constituent elements of the substrate and of the coatings. The calculated *RDS* values are presented in Table 2. One can notice the presence of oxygen and nitrogen in the coatings, as well as a small amount of carbon, probably due to the external handling of samples. A high oxygen content was measured on Cr(N,O) coatings. The low oxygen concentration found in the Cr–N coatings should be treated as contamination, as already reported [62].

Chromium oxynitride coating has a complex structure, its composition and properties being controlled by the deposition parameters, which should ensure the reproducibility of each deposition run. The deposition of chromium oxynitride coating, performed in a mixture of two reactive gases such as O_2 and N_2 , is a complex process due to the different reactivity of the Cr with nitrogen and the more reactive oxygen atoms and ions. The observed increase of O/N ratio—about five-fold—demonstrates the successful deposition of chromium oxynitride coating. The observed significant increase can be ascribed to the higher affinity of Cr for oxygen compared to nitrogen [63].

Table 2. The elemental composition of the monolayered coatings deposited on Si substrates.

Coating	Elemental Composition (at.%)				O/N	O/Cr	(O + N)/Cr
	N	O	Cr	C			
Cr–N	30.5 ± 1.2	2.6 ± 0.2	63.4 ± 2.5	3.5 ± 0.2	0.085	0.041	0.522
Cr(N,O)	35.6 ± 1.7	14.9 ± 0.8	46.8 ± 2.2	2.6 ± 0.1	0.419	0.318	1.079

3.2. Phase Composition

Due to the significant overlapping of 304 SS peaks and those of the deposited coatings (Figure 2a), Figure 2b shows the XRD patterns of the coatings deposited on silicon wafers, discussed as follows. The diffractogram of the Si/Cr–N monolayer presents a shallow peak at 37.7° corresponding to (111)

cubic CrN phase (JCPDS 11-0065, at 37.57°) or to the hexagonal (110) Cr₂N phase (JCPDS 35-0803, at 37.35°). Additionally, a second small peak situated at 43.38° was attributed more probably to the (200) plane of hexagonal Cr₂N phase (JCPDS 35-0803, at 43.40°) than to (200) plane in B1 phase (JCPDS 11-0065, at 43.77°). The high-intensity peak observed at 67.6° was ascribed to the hexagonal Cr₂N phase (JCPDS 35-0803, at 67.3°), suggesting that the deposition conditions favour the formation of a highly-stressed Cr₂N coating. Our results are in good agreement with those reported by Rebholz et al., who showed that in chromium nitride with nitrogen content of about 30 at.%, only Cr₂N phase is present [64], similar to our result (30.5 at.% N). They also showed that both Cr₂N and CrN phases coexist in coatings if the nitrogen content is raised to about 40 at.% [64]. This result is also consistent with the phase diagram of the Cr–N system [65]. Considering the XRD pattern of the coating deposited on SS, one can observe a first broad peak, most probably representing the superposition of the (111) cubic CrN phase and (110) hexagonal Cr₂N phase. The second peak is also broad, higher than the one observed on Si substrate. As such, the presence of (200) planes of the hexagonal Cr₂N and cubic CrN phases is evident from the peak asymmetry. A distinctive feature of the coatings grown on SS is the presence of a third broad peak at about 63° , indicating the overlap of the (211) plane of Cr₂N (JCPDS 35-0803, at 62.44°) and the (220) plane of CrN (JCPDS 11-0065, at 63.60°). Note also that the (300) Cr₂N maximum observed on the Si deposited coating is no longer visible.

In the Cr(N,O) coating deposited on Si, three peaks were observed at 37.9° , 44.2° , and 63.6° , shifted to higher 2θ angles compared to the cubic CrN phase (JCPDS 11-0065, at 37.60° , 43.77° , and 63.60°). The observed shift is due to oxygen incorporation, as also reported by Suzuki et al. for PLD grown Cr(N,O) with different oxygen contents [66]. The observed decrease in the lattice constant and peak shift to higher angles suggests the formation of a solid solution which stabilises the single-phase cubic solid solution of Cr(N,O) [67]. This conclusion is supported by the almost unity value of (N + O)/Cr ratio obtained by EDS. The diffractogram of this coating deposited SS substrate shows the clear signatures of the (200) and (220) planes of Cr(N,O), while the peak ascribed to the (111) plane is not visible. As previously reported, the overall energy contains surface energy and strain energy, and the main coating orientation is correlated with the lower overall energy direction of the films. The presence of only (200) and (220) maxima might be an indication of the surface energy minimisation in Cr(N,O) coating deposited on SS when compared to the one deposited on Si, in which the plane (111) was also present [68,69].

Considering the bilayer coatings, one may observe that the peaks' location was shifted in between the positions observed in Cr–N and Cr(N,O) monolayers, indicating the overlapping of the peaks specific for each monolayer. On the Si/Cr–N/Cr(N,O) diffractogram, one can observe the (111) preferred orientation, as well as the presence of the (300) Cr₂N peak. As the Cr–N layer is located closest to the substrate the peak has a lower intensity, especially in grazing incidence measurement set-up. The diffractogram of SS/Cr–N/Cr(N,O) presents the same peaks as the Si/Cr–N/Cr(N,O), except for the Cr₂N peak (300), which was also missing from that of the SS/Cr–N monolayer.

As expected, in Si/Cr(N,O)/Cr–N bilayer, the Cr₂N peak is more intense, and a (111) significant orientation is present. Moreover, in this bilayer, two diffraction lines were found at 43.3° and 44.3° , ascribed to Cr₂N and Cr(N,O), respectively. As expected, the diffractogram of the SS/Cr(N,O)/Cr–N presents all peaks observed on both SS/Cr–N and SS/Cr(N,O) diffractograms. Summarising the crystalline structures observed in Cr–N/Cr(N,O) coatings deposited on both Si and SS substrates, they are accurately depicting the two composing monolayers. However, the crystalline structures of Si/Cr(N,O)/Cr–N and SS/Cr(N,O)/Cr–N are more complex, as the crystalline Cr(N,O) layer underneath seems to promote the growth of CrN and Cr₂N crystallites in the Cr–N top layer, as it results from the better separated maxima of the two types on chromium nitride.

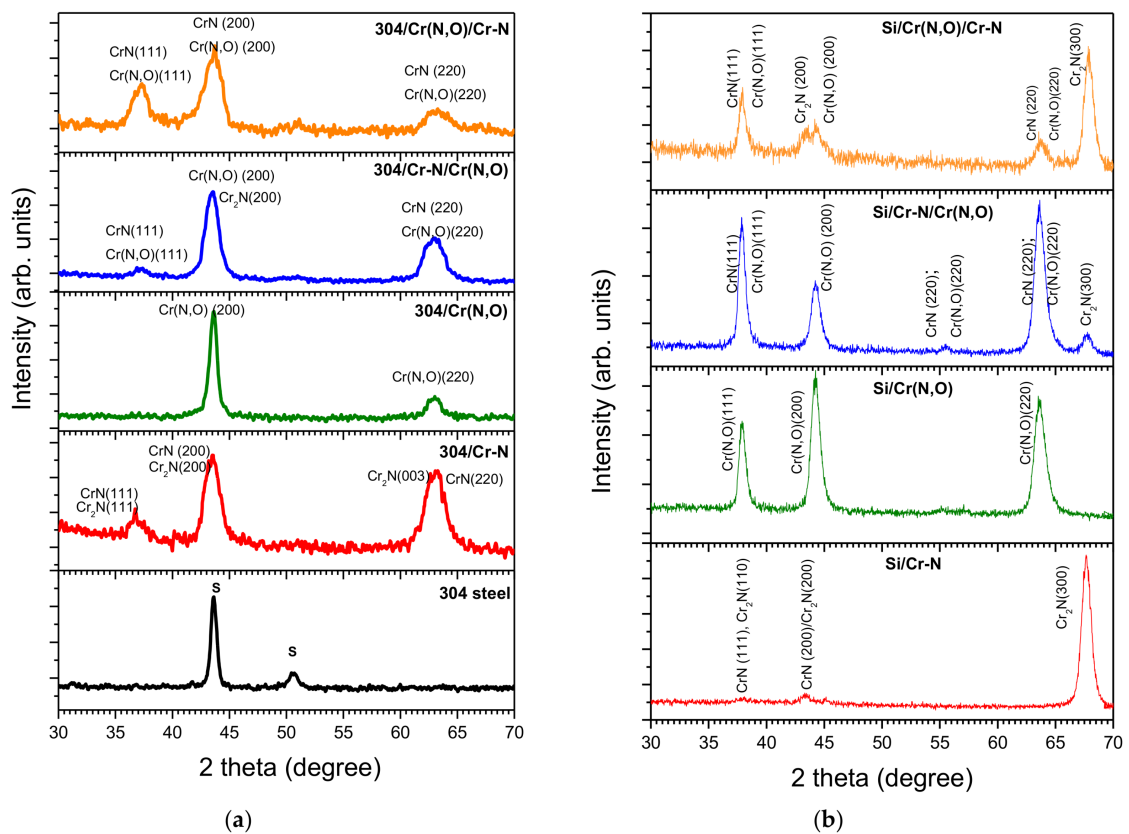


Figure 2. Grazing incidence X-ray diffraction (GI-XRD) patterns of the Cr–N and Cr(N,O) coatings: (a) deposited on stainless steel (SS); (b) deposited on Si.

3.3. Coating Thickness and Roughness

Figure 3 presents, as an example, a profile line of the edge measured on Cr(N,O) coating deposited on the masked Si piece. Additionally, the thickness values of all the investigated coatings are shown.

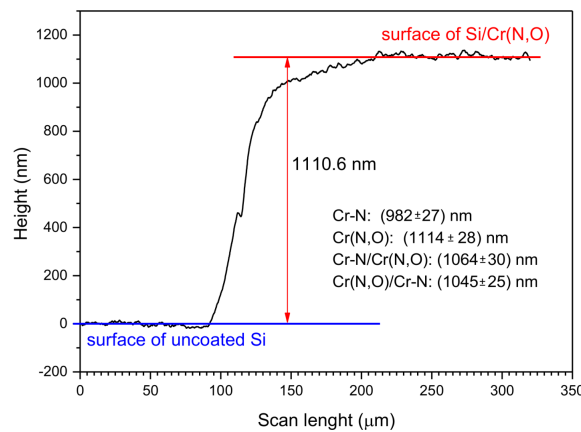


Figure 3. Thickness of the Cr(N,O) coating deposited on Si, measured by surface profilometry, according to the standard DD ENV1071-1:1994, along with all coatings’ thickness values.

The values of the roughness parameters, R_a and R_q , determined for the SS substrate and all deposited coatings, are presented in Figure 4a,b, respectively. One may notice an increase of coating roughness (by a factor of up to approximately 8.5) compared to the bare substrate ($R_a = 48$ nm, $R_q = 60$ nm). In accordance with SEM images, the highest values were obtained for the Cr–N coating:

$R_a = 281.2$ nm, $R_q = 470.6$ nm. This result is due to the observed microdroplets generated from the target material during the reactive cathodic arc deposition, determining the presence of the most numerous peaks. The oxygen addition in the deposition atmosphere slightly decreased the surface roughness, as observed in Cr(N,O) monolayers. In the case of bilayers, considering the errors, the surface roughness is in the same range as that of the oxynitride coating. The observed decrease of the roughness for both bilayers, as compared to the nitride coating, may be ascribed to the lower roughness of Cr(N,O) layer in the bilayer, and to the thinner dimensions of the composing individual layers in the bilayers compared to the monolayer. The trend evidenced for the R_a parameter (Figure 4a) was also preserved for the R_q parameter (Figure 4b).

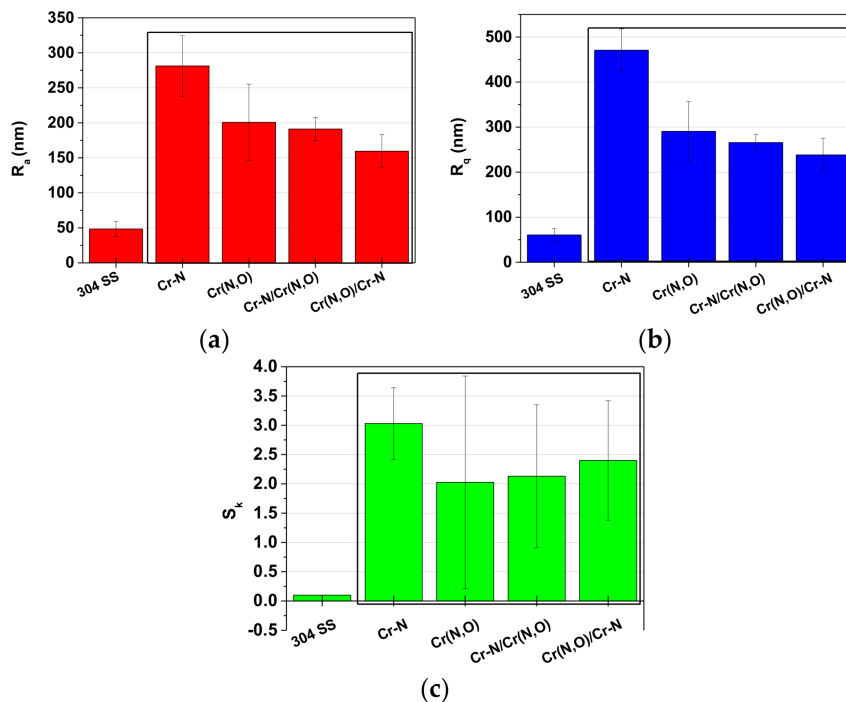


Figure 4. The roughness of Cr-based coatings before the corrosion test: (a) R_a parameter; (b) R_q parameter; (c) S_k parameter.

Since R_a and R_q parameters are not sufficient to evaluate the surface quality, the skewness parameter (S_k) values are presented in Figure 4c. Note the value close to 0 for the SS substrate, indicating a relatively uniform distribution of the peaks and valleys on the surface. The S_k values corresponding to the coatings are in the 2–3 range, indicating the presence of high peaks, since a positive number relates to a higher percentage of profiles situated above the mean line. The presence of these peaks on the surface of coatings is the result of the droplets, as observed by SEM. As mentioned above, this is a characteristic topography of the coatings obtained by the CAE deposition method. It was also reported that other hard coatings (CrN [70], TiN/CrN [71]) deposited by CAE present structural defects on the surface in the form of overgrown droplets, leading to an increased surface roughness, which can affect the corrosion behaviour.

3.4. Coating Mechanical Properties

A coating's functionality is dependent on its superior mechanical properties, which might be the warrant of a prolonged lifetime.

The SEM micrographs of the scratch traces are illustrated in Figure 5. The first sign of coating delamination (L_1) was measured around 10 N loads on the coatings. The highest value, 11.2 N, was obtained for the Cr-N/Cr(N,O) coating.

The Cr(N,O) monolayer was completely delaminated for a load L_2 higher than 19.1 N, while Cr–N coating withstood the gradual increasing loading force up to 23.7 N, denoting an excellent adhesion to the metallic substrate.

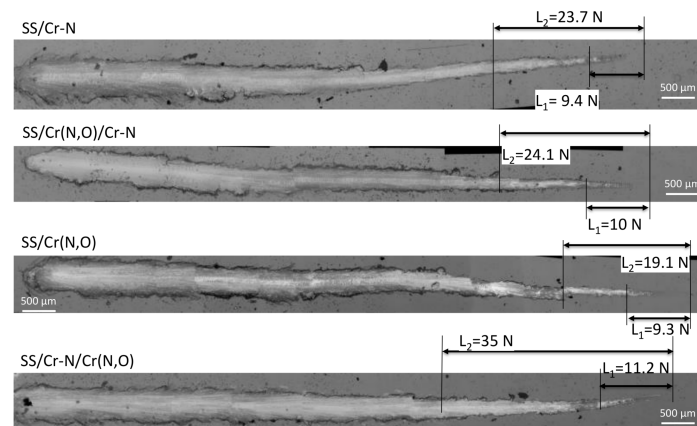


Figure 5. Scratch traces of Cr-based coatings deposited on 304 SS substrate.

Considering the two bilayered coatings, the one containing Cr(N,O) layer at the metal interface presented lower values for both loads (L_1 and L_2), but notably higher than the ones corresponding to Cr(N,O) monolayer. As expected, the presence of Cr–N layer at the metal interface determined the highest values for both L_1 and L_2 (35 N). The best adhesion was measured for the coating Cr–N/Cr(N,O), as a result of the good adhesion of the Cr–N monolayer to the substrate ($L_2 = 23.7$), in comparison with the one exhibited by the Cr(N,O) monolayer ($L_2 = 19.1$ N).

To sum up, both types of bilayer exceeded the delamination load values obtained for monolayers: $L_{1,2}^{\text{Cr(N,O)}} < L_{1,2}^{\text{Cr-N}} < L_{1,2}^{\text{Cr(N,O)/Cr-N}} < L_{1,2}^{\text{Cr-N/Cr(N,O)}}$. The higher adhesion of the two bilayers may be ascribed to the lower internal stress in the bi- and multi-layers, as a reduced intrinsic stress is commonly associated with an enhanced adhesion. Additionally, the presence of a supplementary interface between the two monolayers hinders the crack propagation, determining a better adhesion of the coating to the substrate.

The hardness and reduced elastic modulus of the coatings as determined by nanoindentation are presented in Table 3, and a typical force–displacement curve, with an indentation depth of 67.9 nm—less than 10% of the coating thickness—is presented in Figure 6. As expected, the highest hardness values were obtained for the Cr–N monolayer and for the SS/Cr(N,O)/Cr–N double layer, due to the superior mechanical characteristics of nitrides compared with oxynitrides. However, the aim of the study was to develop corrosion-resistant coatings working under soft erosive conditions. As such, we also looked for superior mechanical properties of the coating, which are related to the various ratios of hardness to reduced elastic modulus [72–74]. It has been reported that H/E_r is related to wear resistance, H^2/E_r to the coating's resilience, and H^3/E_r^2 to plastic deformation resistance, thus it can also predict erosion resistance. As can be observed in Table 3, all these ratios present the same trend as critical load L_2 . The obtained values for H , E_r , and H^3/E_r^2 for Cr–N coating are in agreement with the data previously reported in the literature [75–77].

Table 3. Hardness (H), reduced elastic modulus (E_r), H/E_r , H^3/E_r^2 , H^2/E_r ratios, and the critical loads L_2 , as determined for the Cr-based coatings deposited on 304 SS substrate.

Coating	H (GPa)	ΔH (GPa)	E_r (GPa)	ΔE_r (GPa)	H/E_r	H^3/E_r^2	H^2/E_r	L_2 (N)
SS/Cr–N	24.53	±1.17	227.12	±6.71	0.1080	0.286	2.649	23.7
SS/Cr(N,O)	21.43	±1.70	203.34	±7.95	0.1054	0.238	2.259	19.1
SS/Cr(N,O)/Cr–N	25.28	±1.56	233.57	±8.26	0.1082	0.296	2.736	24.1
SS/Cr–N/Cr(N,O)	22.75	±1.03	175.45	±5.31	0.1296	0.382	2.949	35

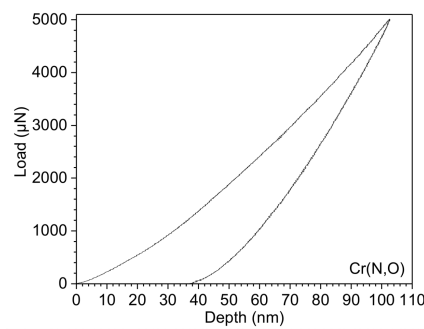


Figure 6. Typical force–displacement curves of Cr(N,O) coating.

3.5. Corrosion Measurements

The open circuit potential evolution during 15 h immersion in 0.10 M NaCl + 1.96 M H₂O₂ is presented in Figure 7. In the first hours of immersion, a slight decrease of potential was observed for all analysed specimens, more pronounced for 304 SS. However, all the coated specimens reached a steady state, the corresponding E_{OC} being in the range 0.02–0.3 V. The stable E_{OC} of the coated specimens is a sign of the probable formation of a stable passivation layer. The slow decrease of the potential corresponding to 304 SS indicates the instability of the passive layer. For the Cr(N,O)/Cr–N bilayer, the initial rapid decrease of the E_{OC} value was followed by a steady increase, such that after 15 h of immersion the value exceeded the one obtained for 304 SS, displaying an increasing tendency up to 117 mV, proving the protective nature of this coating. The most passive layers were formed on the surfaces of the Cr–N/Cr(N,O) and Cr(N,O) coatings, both presenting almost the same variation tendency for E_{OC} , leading to the conclusion that the presence of Cr(N,O) at the point of contact with the corrosive environment has a beneficial effect on the corrosion resistance. In contrast with the above result, the Cr–N monolayer exhibited a better passivation of its surface compared to the Cr(N,O)/Cr–N bilayer, showing an E_{OC} value as low as 0.1 V. This result may be ascribed to the poorer adhesion measured for the Cr(N,O)/Cr–N bilayer. Han and coworkers also studied the corrosion resistance of chromium nitride deposited on low alloy steel (AISI 4140) in an aerated 3% NaCl solution, and reported small negative E_{OC} values (~ -0.7 V), which might be ascribed mainly to the different corrosive environment [78].

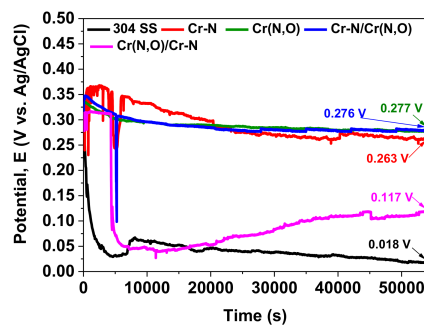


Figure 7. Open circuit potential evolution of Cr-based coatings deposited on 304 SS.

The R_p parameter presented in Table 4 indicates the resistance of the investigated coatings when only a small perturbation was applied (± 10 mV). When compared with the uncoated substrate, all the coatings had a higher R_p value (with a factor of 40 to 106). The bilayer Cr–N/Cr(N,O) exhibited higher polarisation resistance value, followed by the Cr(N,O) monolayer. This result can be explained first by the double layer structure which acts as an enhanced barrier to the ingress of the electrolyte through the surface defects, and secondly by the lower porosity of the Cr(N,O) layer as indicated in Table 4, which further blocked the electrolyte ingress. According to Inoue et al., the oxygen atoms in the Cr(N,O) crystallites diffuse outwards, forming Cr₂O₃ layers which surround the crystallites

and slow down the oxidation speed, such that the oxidation resistivity of Cr(N,O) is increased [67]. No significant differences were found between the Cr–N monolayer and Cr(N,O)/Cr–N bilayer.

Furthermore, E_{corr} and corrosion current density (i_{corr}) were extracted from Tafel plots, as frequently reported (e.g., [79]). Figure 8 shows the Tafel plots for the plain SS substrate and all the coatings deposited on SS. The inset presents the fitting lines for the Cr(N,O) coating. It can be stated that the behaviour of a material is nobler in a corrosive solution, when the corrosion potential (E_{corr}) value is more electropositive. According to Table 4, all coatings were nobler compared to the uncoated substrate. When the Cr(N,O) is used as top layer, the sample has a more electropositive corrosion potential, indicating that the corrosive solution had less influence on these surfaces. Comparing the coating with Cr–N in top, the most noble corrosion potential was measured for Cr–N monolayer, suggesting a good corrosion resistance.

R_p was determined at the open-circuit potential by linear polarisation tests performed by applying a small perturbation (± 10 mV vs. E_{OC}). The R_p values were determined as the slope of the linear region of the $\Delta E - \Delta i$ curve near E_{corr} . The i_{corr} was extracted based on Tafel plots which were recorded from ± 0.25 V vs. E_{OC} , using the corrosion test software (VersaStudio) and performing a numerical fit to the Butler–Volmer equation, as we considered that both a cathodic and an anodic reaction occur on the same electrode. As also indicated by the current density parameter, the coated surfaces are less inclined to allow current to flow, as the i_{corr} parameter was two orders of magnitude lower in value than the SS substrate. Considering this parameter, the Cr(N,O) monolayer showed the lowest i_{corr} , followed by Cr–N/Cr(N,O), Cr(O,N)/Cr–N, and Cr–N coatings. The corrosion rate is proportionally related to the i_{corr} . Thus, we can conclude that the Cr(N,O) monolayer has the lowest corrosion rate. It is interesting to note that the presented Cr–N-based coatings exhibited i_{corr} values lower than the multilayered NbN/CrN coatings with 2 to 10 bilayers, immersed in 0.5 M NaCl solution, deposited by the magnetron sputter deposition, as reported by Aperador and Delgado [80].

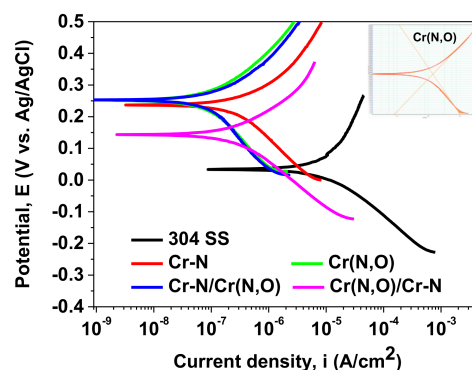


Figure 8. Tafel plots of Cr-based coatings deposited on 304 SS steel; the inset presents the fitting lines in the Tafel plot of Cr(N,O) coating.

Both porosity and protection efficiency of the investigated coatings were calculated based on Equations (2) and (3). By comparing the porosity values, one can conclude that the addition of oxygen leads to a porosity decrease in Cr-based coatings. When the Cr(N,O) layer is on top, it can be seen that the porosity is lower. The Cr(N,O)/Cr–N system shows higher porosity than that Cr–N/Cr(N,O) or Cr(N,O) coatings, its properties being more akin to that of Cr–N.

Regarding the protection efficiency, the best value was found for the Cr(N,O) monolayer, indicating better corrosion resistance. This result is in good agreement with the above-mentioned findings. We note that the Cr(N,O) coating exhibited the best protection efficiency. Moreover, its presence on the top of a bilayer also produced a high protection efficiency, superior to that observed in Cr(N,O)/Cr–N bilayer, probably as a direct result of the beneficial effect of the oxide layers surrounding the crystallites, preventing further oxidation.

Table 4. Corrosion parameters of Cr-based coatings.

Sample	E_{OC} (mV)	R_p (k Ω)	E_{corr} (mV)	i_{corr} (μ A/cm ²)	P	P_e (%)
304 SS	18	2.109	34	14.689	–	–
Cr–N	263	86.136	236	0.492	0.016	96.7
Cr(N,O)	277	187.75	250	0.137	0.007	99.1
Cr(N,O)/Cr–N	117	85.599	143	0.336	0.020	97.7
Cr–N/Cr(N,O)	276	223.047	250	0.168	0.006	98.9

Figure 9a presents the evolution of corrosion current density (i_{corr}) versus the coatings' thickness. One may observe that the increase of coating thickness was accompanied, as expected, by the decrease of i_{corr} and the increase of the protection efficiency, as shown in Figure 9b. The comparison of Cr–N and Cr(N,O)/Cr–N coatings provides evidence that the superior corrosion resistance of the bilayer might be related to its higher adhesion to the substrate and with the presence at the substrate interface of the Cr oxynitride layer, conferring a higher protection efficiency to the bilayer. For the Cr–N/Cr(N,O) bilayer, a small decrease of the protection efficiency and i_{corr} values compared to Cr(N,O) monolayer was evident, despite the modest adhesion performance of the monolayer on SS. Probably the superior corrosion resistance of the Cr(N,O) monolayer might be related to the low roughness, low porosity, and low quantity of microdroplets.

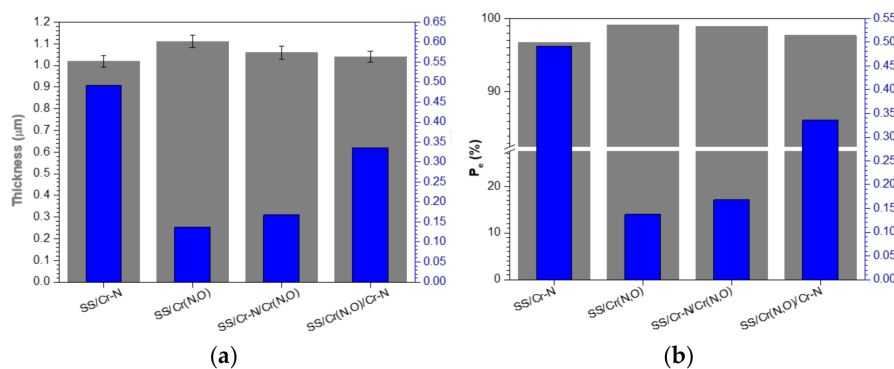


Figure 9. The variation of the corrosion current density (i_{corr}) versus: (a) coatings' thickness; (b) protection efficiency (P_e).

3.6. Characterisation of the Coatings after the Corrosion Tests

3.6.1. Coating Roughness

The roughness of the Cr-based coatings after corrosion tests is presented in Figure 10. The most significant result is related to the roughness increase for all investigated surfaces as a result of corrosive attack, thus we could conclude that all surfaces were affected by the corrosive environment to various extents, as presented in Figure 10 and detailed below.

The roughness parameter R_a of the 304 SS substrate increased from 50 μ m before corrosive attack to about 1300 μ m (Figure 10a), demonstrating that a significant corrosion process affected the bare substrate. The Cr–N monolayer was also considerably affected by corrosion, the R_a increasing from 281 nm (Figure 8a) before corrosion to 549 nm (Figure 10a). This outcome is in good agreement with the electrochemical results, as the R_a value after corrosion increased from 200 nm to 316 nm. On the contrary, the bilayer with Cr(N,O) on top exhibited an almost similar R_a value before and after the corrosive attack, indicating that the roughness was not the main factor influencing the corrosion behaviour. We should underline that within the limit of experimental error, the protection efficiency P_e and the roughness parameters R_a and R_q exhibited the same trend. Moreover, the lower roughness

measured on the bilayered coatings compared to the monolayered ones might be explained by the cracks and dislocation blocking at layer interfaces.

After the corrosion tests, all of the coated surfaces showed negative values of S_k compared to the surfaces before corrosion (Figure 10c), pointing to the formation of more valleys on the corroded surfaces as a consequence of significant corrosive processes taking place locally, where the electric field is more intense due to specific surface morphology. The Cr–N monolayer may well illustrate this conclusion, since compared to all the other coatings, it presented the most negative S_k value and also had the lowest corrosion resistance, as presented in Table 4.

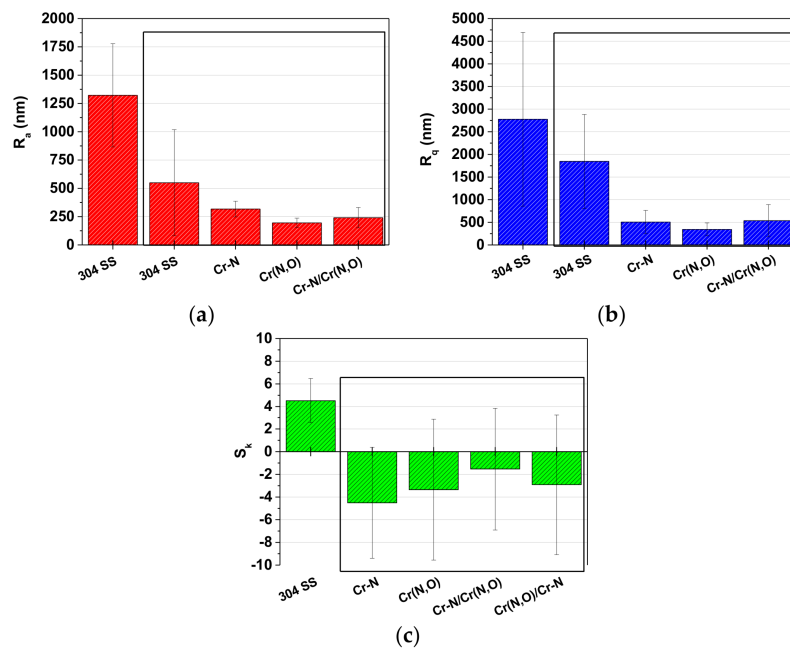


Figure 10. The roughness of Cr-based coatings after the corrosion test: (a) R_a parameter; (b) R_q parameter; (c) S_k parameter.

3.6.2. Surface Morphology and Elemental Composition

In order to gain a deeper insight into the corrosion mechanism in relation to the alteration of the roughness parameters after the corrosion tests, we investigated the surface morphology of corroded surfaces. SEM images of the Cr-based coatings after the corrosion test are presented in Figure 11. As can be seen, the uncoated 304 SS substrate was significantly affected by corrosion, the result being in good agreement with the electrochemical tests. Additionally, the surface of the Cr–N monolayer was deteriorated by the corrosive attack, with numerous damaged zones being observed where the coating was cracked. Some corrosion products were also found on coated surfaces. The poor corrosion resistance of Cr–N monolayer was probably due to the high density of microdroplets and high porosity, confirmed by both SEM images and electrochemical tests, allowing easy chloride penetration and reaching the coating–substrate interface, accelerating the corrosion processes.

According to the electrochemical parameters, the following evolution of corrosion resistance can be stated: Cr(N,O) > Cr–N/Cr(N,O) > Cr(N,O)/Cr–N > Cr–N > SS. By comparing the profilometry lines on selected pits (Figure 11c), it can be seen that the pits found on uncoated 304 SS substrate were deeper and larger than those found on coated surfaces. The Cr(N,O) coating exhibited the best corrosion behaviour, which also showed the small dimensions of pits that appeared during the corrosion tests. This result supports the electrochemical results.

Figure 12 shows the EDS mapping of the damaged zone found on each investigated coating after the corrosion tests. The elemental compositions of the coatings on SS substrates before and after the corrosion tests are presented in Table 5. A low content of the substrate's elements was found in coatings

with high corrosion resistance, such as Cr(N,O) monolayer and Cr-N/Cr(N,O) bilayer. The highest amount of Fe originating from the substrate was detected on the Cr-N monolayer surface, confirming that this coating was significantly affected by the corrosion. In conclusion, the results obtained from SEM and EDS analyses carried out on corroded surfaces sustain the electrochemical results.

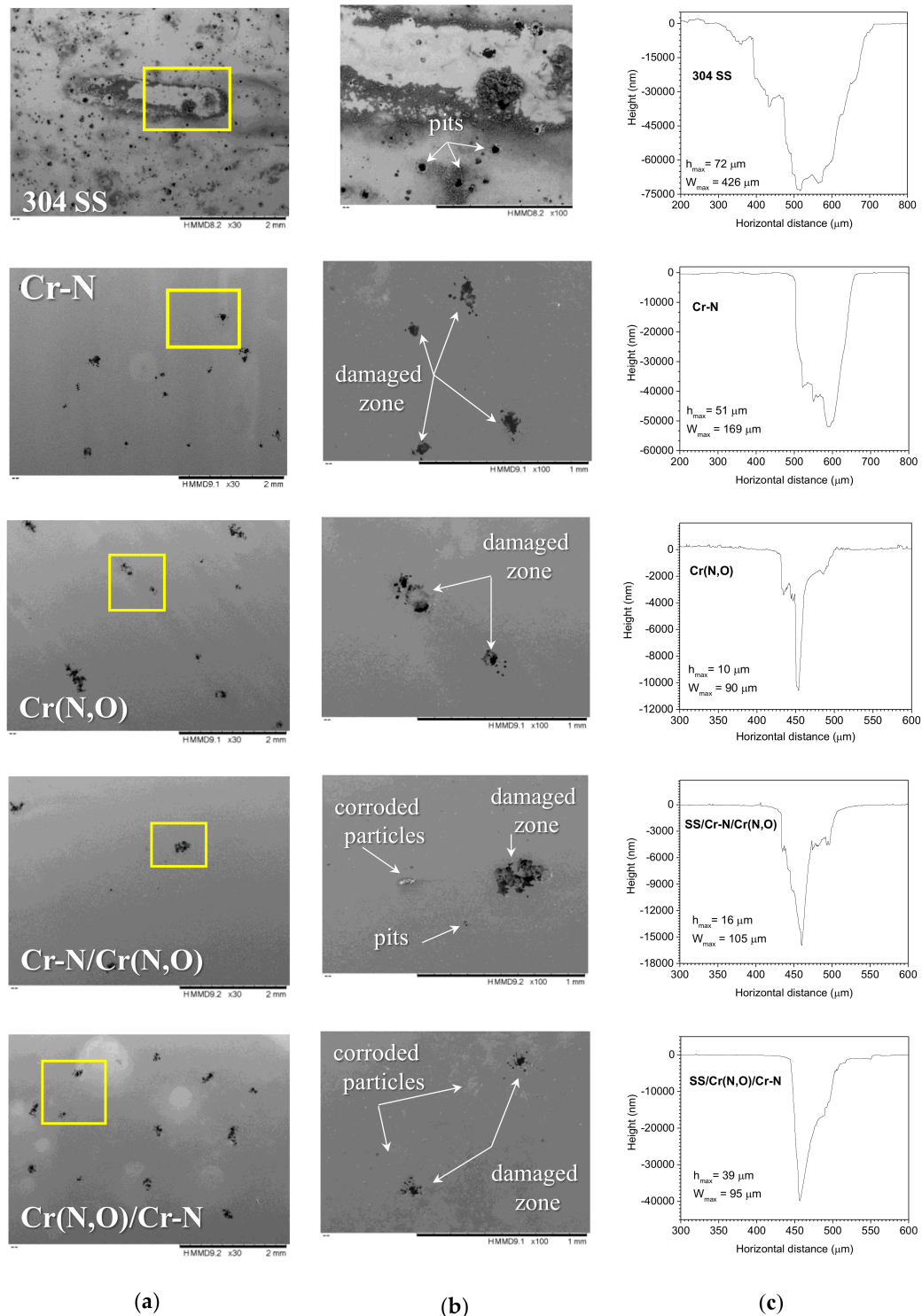


Figure 11. Investigation of the Cr-based coatings surfaces after the corrosion tests: micrographs of: (a) SEM micrographs at 30× magnification; (b) SEM micrographs at 100× magnification; (c) profilometry lines on selected pits.

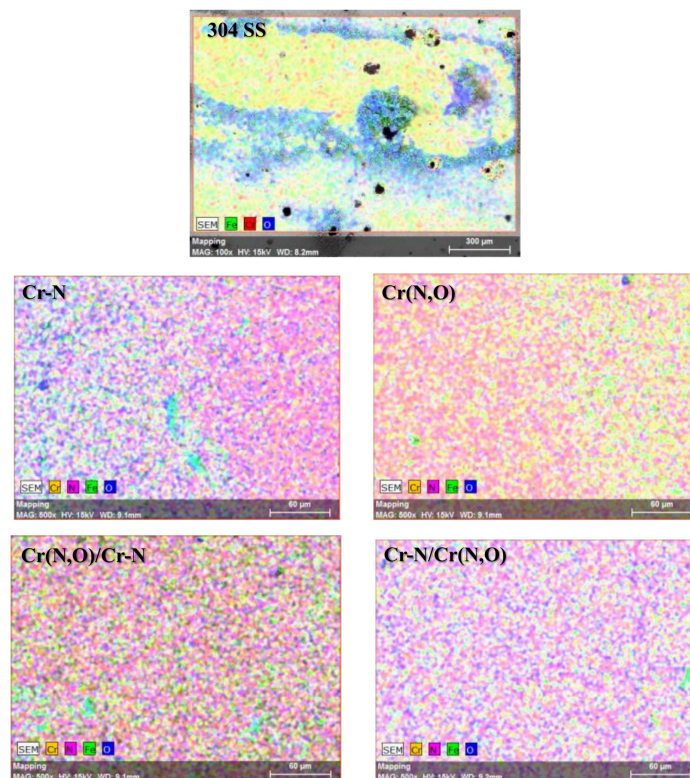


Figure 12. Energy dispersive X-ray spectrometry (EDS) mapping micrographs of the Cr-based coatings after the corrosion test.

Table 5. The elemental composition of the investigated specimens before (B) and after (A) the corrosion test in the areas shown in Figure 11a.

Substrate/Coating (Image Zone)	Elemental Composition (at.%)				
	N	O	Cr	C	Fe
304 SS (A)	–	41.0 ± 2.8	9.5 ± 0.1	–	49.5 ± 3.2
Cr–N (B)	30.5 ± 1.2	2.6 ± 0.2	63.4 ± 2.5	3.5 ± 0.2	–
Cr–N (A)	22.7 ± 0.8	17.5 ± 0.1	56.8 ± 1.8	–	3.0 ± 0.1
Cr(N,O) (B)	35.6 ± 1.7	14.9 ± 0.8	46.8 ± 2.2	2.6 ± 0.1	–
Cr(N,O) (A)	32.4 ± 1.5	20.2 ± 0.3	46.2 ± 2.1	–	1.2 ± 0.1
Cr–N/ Cr(N,O) (B)	36.9 ± 1.7	13.5 ± 0.7	49.3 ± 2.2	2.2 ± 0.1	–
Cr–N/ Cr(N,O) (A)	35.8 ± 1.5	17.4 ± 0.8	46.6 ± 1.8	–	0.5 ± 0.1
Cr(N,O)/Cr–N (B)	31.5 ± 1.3	2.8 ± 0.2	61.5 ± 2.5	4.2 ± 0.2	–
Cr(N,O)/Cr–N (A)	31.1 ± 1.3	22.9 ± 1.3	44.1 ± 2.1	–	1.9 ± 0.1

4. Conclusions

Cr-based coatings in monolayered (Cr–N and Cr(N,O)) and bilayered structures (Cr–N/Cr(N,O) and Cr(N,O)/Cr–N) were prepared by the cathodic arc method. The presence of Cr₂N, CrN, and Cr(N,O), as well as mixtures of these phases were identified and related to the composition of coatings. The oxynitrides were smooth, compact, and homogeneously deposited on 304 SS, with few microdroplets. The corrosion protection performance of the developed mono- and bilayered Cr-based coatings was evaluated in 0.10 M NaCl + 1.96 M H₂O₂.

- The corrosion current densities of the coatings decreased by more than 30 times compared to the bare substrate.
- The Cr–N coating, as mono- or bilayer, had high porosity and lower protective performance.

- The protective efficiency of Cr(N,O) coating (99.1%) and porosity (0.007) were excellent when compared to other coatings, because this coating is denser, less porous, and more adherent to the substrate.
- Both bilayer coatings substantially improved the corrosion protection of 304 SS.
- The bilayer with Cr(N,O) on top possessed the best corrosion resistance behaviour, having the lowest current density corrosion and consequently the highest protective efficiency and the lowest porosity.
- The corrosion resistance can be ranked in the following order: Cr(N,O) > Cr-N/Cr(N,O) > Cr(N,O)/Cr-N > Cr-N.

Acknowledgments: The authors are grateful for the financial support of a grant of the Bilateral Cooperation South Africa–Romania Projects (no. PN-II-CT-RO-ZA-2014-1 and NRF project reference no. UID: 104018, as acknowledged by NRF/RISA Reference RJCT14042566606) signed between the Romanian National Authority for Scientific Research and Innovation, CNCS-UEFISCDI and the South Africa National Research Foundation. The work has also been funded by the Core Program PN 2018, under the support of the Romanian Ministry of Research and Innovation. The EDS, SEM, and XRD results were obtained using the systems purchased by the Romanian Sectorial Operational Programme “Increase of economic Competitiveness”, ID 1799/SMIS 48589/2015.

Author Contributions: M.B. and L.F.P. designed the research and supervised the work; M.D., A.C.P. and E.S.M.M. performed the experiments; A.V. prepared the coatings. M.D. and A.V. analysed the data and provided valuable input in data interpretation; M.D., E.S.M.M. and A.V. wrote the first draft of the article; all authors reviewed and approved the work.

Conflicts of Interest: The authors declare no conflict of interest. The founding sponsors had no role in the design of the study; in the collection, analyses, or interpretation of data; in the writing of the manuscript, and in the decision to publish the results.

References

1. Baddoo, N.R. Stainless steel in construction: A review of research, applications, challenges and opportunities. *J. Constr. Steel Res.* **2008**, *64*, 1199–1206. [[CrossRef](#)]
2. Disegi, J.A.; Eschbach, L. Stainless steel in bone surgery. *Injury* **2000**, *31*, D2–D6. [[CrossRef](#)]
3. *Handbook of Stainless Steel*; Outokumpu: Helsinki, Finland, 2013.
4. Gedge, G. Structural uses of stainless steel—Buildings and civil engineering. *J. Constr. Steel Res.* **2008**, *64*, 1194–1198. [[CrossRef](#)]
5. Pocaznoi, D.; Calmet, A.; Etcheverry, L.; Erable, B.; Bergel, A. Stainless steel is a promising electrode material for anodes of microbial fuel cells. *Energy Environ. Sci.* **2012**, *5*, 9645–9652. [[CrossRef](#)]
6. Park, S.H.C.; Sato, Y.S.; Kokawa, H.; Okamoto, K.; Hirano, S.; Inagaki, M. Corrosion resistance of friction stir welded 304 stainless steel. *Scr. Mater.* **2004**, *51*, 101–105. [[CrossRef](#)]
7. Arango, S.; Peláez-Vargas, A.; García, C. Coating and surface treatments on orthodontic metallic materials. *Coatings* **2013**, *3*, 1–15. [[CrossRef](#)]
8. Hao, L.; Yoshida, H.; Itoi, T.; Lu, Y. Preparation of metal coatings on steel balls using mechanical coating technique and its process analysis. *Coatings* **2017**, *7*, 53. [[CrossRef](#)]
9. Mohamed, A.M.A.; Abdullah, A.M.; Younan, N.A. Corrosion behavior of superhydrophobic surfaces: A review. *Arab. J. Chem.* **2015**, *8*, 749–765. [[CrossRef](#)]
10. Perillo, P.M. Corrosion behavior of coatings of titanium nitride and titanium-titanium nitride on steel substrates. *Corrosion* **2006**, *62*, 182–185. [[CrossRef](#)]
11. Wicks, Z.W.; Jones, F.N.; Pappas, S.P.; Wicks, D.A. Corrosion protection by coatings. *Org. Coat.* **2007**, 137–158. [[CrossRef](#)]
12. Khelifa, F.; Habibi, Y.; Benard, F.; Dubois, P. Smart acrylic coatings containing silica particles for corrosion protection of aluminum and other metals. In *Handbook of Smart Coatings for Materials Protection*; Makhoulouf, A.S.H., Ed.; Elsevier: Amsterdam, The Netherlands, 2014; pp. 423–458. [[CrossRef](#)]
13. Montemor, M.F. Functional and smart coatings for corrosion protection: A review of recent advances. *Surf. Coat. Technol.* **2014**, *258*, 17–37. [[CrossRef](#)]
14. Fenker, M.; Balzer, M.; Kappl, H. Corrosion protection with hard coatings on steel: Past approaches and current research efforts. *Surf. Coat. Technol.* **2014**, *257*, 182–205. [[CrossRef](#)]

15. Verran, J.; Packer, A.; Kelly, P.; Whitehead, K.A. Titanium-coating of stainless steel as an aid to improved cleanability. *Int. J. Food Microbiol.* **2010**, *141*, S134–S139. [[CrossRef](#)] [[PubMed](#)]
16. Mackey, E.D.; Seacord, T.F. Guidelines for using stainless steel in the water and desalination industries. *J. Am. Water Works Assoc.* **2017**, *109*, E158–E169. [[CrossRef](#)]
17. Theodore, N.D.; Holloway, B.C.; Manos, D.M.; Moore, R.; Hernandez, C.; Wang, T.; Dylla, H.F. Nitrogen-implanted silicon oxynitride: A coating for suppressing field emission from stainless steel used in high-voltage applications. *IEEE Trans. Plasma Sci.* **2006**, *34*, 1074–1079. [[CrossRef](#)]
18. Zalnezhad, E.; Hamouda, A.M.S.; Faraji, G.; Shamshirband, S. TiO₂ nanotube coating on stainless steel 304 for biomedical applications. *Ceram. Int.* **2015**, *41*, 2785–2793. [[CrossRef](#)]
19. Shaigan, N.; Qu, W.; Ivey, D.G.; Chen, W. A review of recent progress in coatings, surface modifications and alloy developments for solid oxide fuel cell ferritic stainless steel interconnects. *J. Power Sources* **2010**, *195*, 1529–1542. [[CrossRef](#)]
20. Pruncu, C.I.; Braic, M.; Dearn, K.D.; Farcau, C.; Watson, R.; Constantin, L.R.; Balaceanu, M.; Braic, V.; Vladescu, A. Corrosion and tribological performance of quasi-stoichiometric titanium containing carbo-nitride coatings. *Arab. J. Chem.* **2016**, *10*, 1015–1028. [[CrossRef](#)]
21. Sperko, W.J. *Rust on Stainless Steel*; Sperko Engineering Services Inc.: Greensboro, NC, USA, 2014.
22. Muslim, Z.R.; Abbas, A.A. The effect of pH and temperature on corrosion rate stainless steel 316L used as biomaterial. *Int. J. Basic Appl. Sci.* **2012**, *4*, 17–20.
23. Truman, J.E. The influence of chloride content, pH and temperature of test solution on the occurrence of stress corrosion cracking with austenitic stainless steel. *Corros. Sci.* **1977**, *17*, 737–746. [[CrossRef](#)]
24. Vitelaru, C.; Balaceanu, M.; Parau, A.; Luculescu, C.R.; Vladescu, A. Investigation of nanostructured TiSiC-Zr and TiSiC-Cr hard coatings for industrial applications. *Surf. Coat. Technol.* **2014**, *251*, 21–28. [[CrossRef](#)]
25. Yun, J.S.; Hong, Y.S.; Kim, K.H.; Kwon, S.H.; Wang, Q.M. Characteristics of Ternary Cr-O-N Coatings Synthesized by Using an Arc Ion Plating Technique. *J. Korean Phys. Soc.* **2010**, *57*, 103.
26. Chen, S.; Wu, B.H.; Xie, D.; Jiang, F.; Liu, J.; Sun, H.L.; Zhu, S.; Bai, B.; Leng, Y.X.; Huang, N.; et al. The adhesion and corrosion resistance of Ti–O films on CoCrMo alloy fabricated by high power pulsed magnetron sputtering (HPPMS). *Surf. Coat. Technol.* **2014**, *252*, 8–14. [[CrossRef](#)]
27. Ryabchikov, A.I.; Ryabchikov, I.A.; Stepanov, I.B. Development of filtered DC metal plasma ion implantation and coating deposition methods based on high-frequency short-pulsed bias voltage application. *Vacuum* **2005**, *78*, 331–336. [[CrossRef](#)]
28. Ryabchikov, A.I.; Ryabchikov, I.A.; Stepanov, I.B.; Usov, Y.P. High-frequency short-pulsed metal plasma-immersion ion implantation or deposition using filtered DC vacuum-arc plasma. *Surf. Coat. Technol.* **2007**, *201*, 6523–6525. [[CrossRef](#)]
29. Ryabchikov, A.I.; Ryabchikov, I.A.; Stepanov, I.B.; Sivina, D.O. Recent advances in surface processing with the filtered DC vacuum-arc plasma. *Vacuum* **2005**, *78*, 445–449. [[CrossRef](#)]
30. Ryabchikov, A.I.; Ryabchikov, I.A.; Stepanov, I.B.; Dektyarev, S.V. High current vacuum-arc ion source for ion implantation and coating deposition technologies. *Rev. Sci. Instrum.* **2006**, *77*, 03B516. [[CrossRef](#)]
31. Stepanov, I.B.; Ryabchikov, A.I.; Nochovnaya, N.A.; Sharkeev, Y.P.; Shulepov, I.A.; Ryabchikov, I.A.; Sivina, D.O.; Fortuna, S.V. Vacuum arc filtered metal plasma application in hybrid technologies of ion-beam and plasma material processing. *Surf. Coat. Technol.* **2007**, *201*, 8596–8600. [[CrossRef](#)]
32. Davis, J. *Corrosion: Understanding the Basics*; ASM International: Geauga County, OH, USA, 2000; p. 574.
33. Estrada-Martínez, J.; Reyes-Gasga, J.; García-García, R.; Vargas-Becerril, N.; Zapata-Torres, M.G.; Gallardo-Rivas, N.V.; Mendoza-Martínez, A.M.; Paramo-García, U. Wettability modification of the AISI 304 and 316 stainless steel and glass surfaces by titanium oxide and titanium nitride coating. *Surf. Coat. Technol.* **2017**, *330*, 61–70. [[CrossRef](#)]
34. Ali, F.; Kwak, J.S. The impact of number of interfaces on corrosion behavior of TiCrN films. *J. Nanosci. Nanotechnol.* **2017**, *17*, 4318–4321. [[CrossRef](#)]
35. Adesina, A.Y.; Gasem, Z.M.; Madhan Kumar, A. Corrosion resistance behavior of single-layer cathodic arc PVD nitride-base coatings in 1M HCl and 3.5 pct NaCl Solutions. *Metall. Mater. Trans. B Process Metall. Mater. Process. Sci.* **2017**, *48*, 1321–1332. [[CrossRef](#)]
36. Navinsek, B.; Seal, S. Transition metal nitride functional coatings. *JOM* **2001**, *53*, 51–54. [[CrossRef](#)]

37. Mayrhofer, P.H.; Rachbauer, R.; Holec, D.; Rovere, F.; Schneider, J.M. Protective transition metal nitride coatings. In *Comprehensive Materials Processing*; Hashmi, S., Ed.; Elsevier: Amsterdam, The Netherlands, 2014; Volume 4, pp. 355–388, ISBN 9780080965338.
38. Braic, L.; Vasilantonakis, N.; Mihai, A.; Garcia, I.J.V.; Fearn, S.; Zou, B.; Alford, N.M.; Doiron, B.; Oulton, R.F.; Maier, S.A.; et al. Titanium oxynitride thin films with tunable double epsilon-near-zero behavior for nanophotonic applications. *ACS Appl. Mater. Interfaces* **2017**, *9*, 29857–29862. [[CrossRef](#)] [[PubMed](#)]
39. Fenker, M.; Kappl, H.; Carvalho, P.; Vaz, F. Thermal stability, mechanical and corrosion behaviour of niobium-based coatings in the ternary system Nb–O–N. *Thin Solid Films* **2011**, *519*, 2457–2463. [[CrossRef](#)]
40. Braic, M.; Balaceanu, M.; Vladescu, A.; Kiss, A.; Braic, V.; Epurescu, G.; Dinescu, G.; Moldovan, A.; Birjega, R.; Dinescu, M. Preparation and characterization of titanium oxy-nitride thin films. *Appl. Surf. Sci.* **2007**, *253*, 8210–8214. [[CrossRef](#)]
41. Subramanian, B.; Muraleedharan, C.V.; Ananthakumar, R.; Jayachandran, M. A comparative study of titanium nitride (TiN), titanium oxy nitride (TiON) and titanium aluminum nitride (TiAlN), as surface coatings for bio implants. *Surf. Coat. Technol.* **2011**, *205*, 5014–5020. [[CrossRef](#)]
42. Rtimi, S.; Baghriche, O.; Sanjines, R.; Pulgarin, C.; Bensimon, M.; Kiwi, J. TiON and TiON-Ag sputtered surfaces leading to bacterial inactivation under indoor actinic light. *J. Photochem. Photobiol. A Chem.* **2013**, *256*, 52–63. [[CrossRef](#)]
43. Li, W.Z.; Yi, D.Q.; Li, Y.Q.; Liu, H.Q.; Sun, C. Effects of the constitution of CrON diffusion barrier on the oxidation resistance and interfacial fracture of duplex coating system. *J. Alloys Compd.* **2012**, *518*, 86–95. [[CrossRef](#)]
44. Li, W.Z.; Yao, Y.; Wang, Q.M.; Bao, Z.B.; Gong, J.; Sun, C.; Jiang, X. Improvement of oxidation-resistance of NiCrAlY coatings by application of CrN or CrON interlayer. *J. Mater. Res.* **2011**, *23*, 341–352. [[CrossRef](#)]
45. Warcholinski, B.; Gilewicz, A.; Lupicka, O.; Kuprin, A.S.; Tolmachova, G.N.; Ovcharenko, V.D.; Kolodiy, I.V.; Sawczak, M.; Kochmanska, A.E.; Kochmanski, P.; et al. Structure of CrON coatings formed in vacuum arc plasma fluxes. *Surf. Coat. Technol.* **2016**, *309*, 920–930. [[CrossRef](#)]
46. Cubillos, G.I.; Bethencourt, M.; Olaya, J.J.; Alfonso, J.E.; Marco, J.F. The influence of deposition temperature on microstructure and corrosion resistance of ZrO_xN_y/ZrO₂ coatings deposited using RF sputtering. *Appl. Surf. Sci.* **2014**, *309*, 181–187. [[CrossRef](#)]
47. Tijani, J.O.; Mouele, M.E.S.; Tottito, T.C.; Fatoba, O.O.; Petrik, L.F. Degradation of 2-nitrophenol by dielectric barrier discharge system: The Influence of carbon doped TiO₂ photocatalyst supported on stainless steel mesh. *Plasma Chem. Plasma Process.* **2017**, *37*, 1343–1373. [[CrossRef](#)]
48. Ruden, A.; Restrepo-Parra, E.; Paladines, A.U.; Sequeda, F. Corrosion resistance of CrN thin films produced by dc magnetron sputtering. *Appl. Surf. Sci.* **2013**, *270*, 150–156. [[CrossRef](#)]
49. Wang, D.; Hu, M.; Jiang, D.; Fu, Y.; Wang, Q.; Yang, J.; Sun, J.; Weng, L. The improved corrosion resistance of sputtered CrN thin films with Cr-ion bombardment layer by layer. *Vacuum* **2017**, *143*, 329–335. [[CrossRef](#)]
50. Chen, Q.; Cao, Y.; Xie, Z.; Chen, T.; Wan, Y.; Wang, H.; Gao, X.; Chen, Y.; Zhou, Y.; Guo, Y. Tribocorrosion behaviors of CrN coating in 3.5 wt.% NaCl solution. *Thin Solid Films* **2017**, *622*, 41–47. [[CrossRef](#)]
51. Shan, L.; Zhang, Y.R.; Wang, Y.X.; Li, J.L.; Jiang, X.; Chen, J.M. Corrosion and wear behaviors of PVD CrN and CrSiN coatings in seawater. *Trans. Nonferrous Met. Soc. China* **2016**, *26*, 175–184. [[CrossRef](#)]
52. Ma, F.; Li, J.; Zeng, Z.; Gao, Y. Structural, mechanical and tribocorrosion behaviour in artificial seawater of CrN/AlN nano-multilayer coatings on F690 steel substrates. *Appl. Surf. Sci.* **2018**, *428*, 404–414. [[CrossRef](#)]
53. Gulbiński, W.; Gilewicz, A.; Suszko, T.; Warcholiński, B.; Kukliński, Z. Ti–Si–C sputter deposited thin film coatings. *Surf. Coat. Technol.* **2004**, *180–181*, 341–346. [[CrossRef](#)]
54. Gilewicz, A.; Chmielewska, P.; Murzynski, D.; Dobruchowska, E.; Warcholinski, B. Corrosion resistance of CrN and CrCN/CrN coatings deposited using cathodic arc evaporation in Ringer's and Hank's solutions. *Surf. Coat. Technol.* **2016**, *299*, 7–14. [[CrossRef](#)]
55. Dinu, M.; Hauffman, T.; Cordioli, C.; Vladescu, A.; Braic, M.; Hubin, A.; Cotrut, C.M. Protective performance of Zr and Cr based silico-oxynitrides used for dental applications by means of potentiodynamic polarization and odd random phase multisine electrochemical impedance spectroscopy. *Corros. Sci.* **2017**, *115*, 118–128. [[CrossRef](#)]
56. Piedrahita, W.F.; Coy, L.E.; Amaya, C.; Llarena, I.; Caicedo, J.C.; Yate, L. Influence of the negative R.F. bias voltage on the structural, mechanical and electrical properties of Hf–C–N coatings. *Surf. Coat. Technol.* **2016**, *286*, 251–255. [[CrossRef](#)]

57. BS EN 1071-3:2005 *Advanced Technical Ceramics—Methods of Test for Ceramic Coatings*; British Standards Institution: London, UK, 2005; p. 47.
58. Oliver, W.C.; Pharr, G.M. An improved technique for determining hardness and elastic modulus using load and displacement sensing indentation experiments. *J. Mater. Res.* **1992**, *6*, 1564–1583. [[CrossRef](#)]
59. Li, M.S.; Feng, C.J.; Wang, F.H. Effect of partial pressure of reactive gas on chromium nitride and chromium oxide deposited by arc ion plating. *Trans. Nonferrous Met. Soc. China* **2006**, *16*, s276–s279. [[CrossRef](#)]
60. Münz, W.-D.; Smith, I.J.; Lewis, D.B.; Creasey, S. Droplet formation on steel substrates during cathodic steered arc metal ion etching. *Vacuum* **1997**, *48*, 473–481. [[CrossRef](#)]
61. Massalski, T.B.; Okamoto, H.; Subramanian, P.R.; Kacprzak, L. *Binary Alloy Phase Diagrams*, 2nd ed.; ASM International: Geauga County, OH, USA, 1990.
62. Ehrlich, A.; Kühn, M.; Richter, F.; Hoyer, W. Complex characterisation of vacuum arc-deposited chromium nitride thin films. *Surf. Coat. Technol.* **1995**, *76–77*, 280–286. [[CrossRef](#)]
63. Minami, T.; Nishio, S.; Murata, Y. Periodic microstructures of Cr–O–N coatings deposited by arc ion plating. *Surf. Coat. Technol.* **2014**, *254*, 402–409. [[CrossRef](#)]
64. Rebholz, C.; Ziegele, H.; Leyland, A.; Matthews, A. Structure, mechanical and tribological properties of nitrogen-containing chromium coatings prepared by reactive magnetron sputtering. *Surf. Coat. Technol.* **1999**, *115*, 222–229. [[CrossRef](#)]
65. Anna, E.M.; McMurdie, H.F.; Ondik, H.M. Borides carbides and nitrides. In *Phase Equilibria Diagrams*; McHale, A.E., Ed.; The American Ceramic Society: Westerville, OH, USA, 1994; p. 415.
66. Suzuki, K.; Endo, T.; Fukushima, T.; Sato, A.; Suzuki, T.; Nakayama, T.; Suematsu, H.; Niihara, K. Controlling oxygen content by varying oxygen partial pressure in chromium oxynitride thin films prepared by pulsed laser deposition. *Mater. Trans.* **2013**, *54*, 1140–1144. [[CrossRef](#)]
67. Suzuki, K.; Endo, T.; Sato, A.; Suzuki, T.; Nakayama, T.; Suematsu, H.; Niihara, K. Epitaxial growth of chromium oxynitride thin films on magnesium oxide (100) substrates and their oxidation behavior. *Mater. Trans.* **2013**, *54*, 1957–1961. [[CrossRef](#)]
68. Oh, U.C.; Je, J.H. Effects of strain energy on the preferred orientation of TiN thin films. *J. Appl. Phys.* **1993**, *74*, 1692–1696. [[CrossRef](#)]
69. Pelleg, J.; Zevin, L.Z.Z.; Lungo, S.; Croitoru, N. Reactive-sputter-deposited TiN films on glass substrates. *Thin Solid Films* **1991**, *197*, 117–128. [[CrossRef](#)]
70. Sebastiani, M.; Piccoli, M.; Bemporad, E. Effect of micro-droplets on the local residual stress field in CAE-PVD thin coatings. *Surf. Coat. Technol.* **2013**, *215*, 407–412. [[CrossRef](#)]
71. Steyer, P.; Mege, A.; Pech, D.; Mendibide, C.; Fontaine, J.; Pierson, J.F.; Esnouf, C.; Goudeau, P. Influence of the nanostructuring of PVD hard TiN-based films on the durability of coated steel. *Surf. Coat. Technol.* **2008**, *202*, 2268–2277. [[CrossRef](#)]
72. Musil, J.; Novák, P.; Čerstvý, R.; Soukup, Z. Tribological and mechanical properties of nanocrystalline-TiC/a-C nanocomposite thin films. *J. Vac. Sci. Technol. A Vac. Surf. Film* **2010**, *28*, 244–249. [[CrossRef](#)]
73. Yate, L.; Martínez-de-Olcoz, L.; Esteve, J.; Lousa, A. Ultra low nanowear in novel chromium/amorphous chromium carbide nanocomposite films. *Appl. Surf. Sci.* **2017**, *420*, 707–713. [[CrossRef](#)]
74. Castanho, J.M.; Vieira, M.T. Effect of ductile layers in mechanical behaviour of TiAlN thin coatings. *J. Mater. Process. Technol.* **2003**, *143–144*, 352–357. [[CrossRef](#)]
75. Mohammadpour, E.; Jiang, Z.-T.; Altarawneh, M.; Mondinos, N.; Rahman, M.M.; Lim, H.N.; Huang, N.M.; Xie, Z.; Zhou, Z.; Dlugogorski, B.Z. Experimental and predicted mechanical properties of Cr_{1-x}Al_xN thin films, at high temperatures, incorporating in situ synchrotron radiation X-ray diffraction and computational modelling. *RSC Adv.* **2017**, *7*, 22094–22104. [[CrossRef](#)]
76. Jagielski, J.; Khanna, A.S.; Kucinski, J.; Mishra, D.S.; Racolta, P.; Sioshansi, P.; Tobin, E.; Thereska, J.; Uglov, V.; Vilaithong, T.; et al. Effect of chromium nitride coating on the corrosion and wear resistance of stainless steel. *Appl. Surf. Sci.* **2000**, *156*, 47–64. [[CrossRef](#)]
77. Han, S.; Lin, J.H.; Tsai, S.H.; Chung, S.C.; Wang, D.Y.; Lu, F.H.; Shih, H.C. Corrosion and tribological studies of chromium nitride coated on steel with an interlayer of electroplated chromium. *Surf. Coat. Technol.* **2000**, *133–134*, 460–465. [[CrossRef](#)]
78. Han, S.; Lin, J.H.; Wang, D.Y.; Lu, F.-H.; Shih, H.C. Corrosion resistance of chromium nitride on low alloy steels by cathodic arc deposition. *J. Vac. Sci. Technol. Part A Vac. Surf. Film* **2001**, *19*, 1442–1446. [[CrossRef](#)]

79. Yate, L.; Coy, L.E.; Aperador, W. Robust tribo-mechanical and hot corrosion resistance of ultra-refractory Ta–Hf–C ternary alloy films. *Sci. Rep.* **2017**, *7*, 3080. [[CrossRef](#)] [[PubMed](#)]
80. Aperador, W.; Duque, J.; Delgado, E. Electrochemical and tribological and mechanical performances coatings multilayer type NbC/CrN. *Int. J. Electrochem. Sci.* **2016**, *11*, 6347–6355. [[CrossRef](#)]



© 2018 by the authors. Licensee MDPI, Basel, Switzerland. This article is an open access article distributed under the terms and conditions of the Creative Commons Attribution (CC BY) license (<http://creativecommons.org/licenses/by/4.0/>).